Research in Astronomy and Astrophysics, 25:055009 (18pp), 2025 May

https://doi.org/10.1088/1674-4527/adc85c
CSTR: 32081.14.RAA.adc85c

Unveiling the Quenching Mode of Dwarf Galaxies Beyond Redshift $z = 1$ with JWST Image Stacking

Yubin Li[1,2,3], Nan Li[2,3], Fengshan Liu[2,3], Jirong Mao[1,2], Qifan Cui[3,4], Jian Ren[3], Pinsong Zhao[3,5], Hao Mo[2,3], Qi Song[3], and Xin Zhang[3]

[1] Yunnan Observatories, Chinese Academy of Sciences, Kunming 650216, China; jirongmao@mail.ynao.ac.cn
[2] University of Chinese Academy of Sciences, Beijing 100049, China; nan.li@nao.cas.cn, fsliu@nao.cas.cn
[3] National Astronomical Observatories, Chinese Academy of Sciences, Beijing 100101, China
[4] Shanghai Key Lab for Astrophysics, Shanghai Normal University, Shanghai 200234, China
[5] Kavli Institute for Astronomy and Astrophysics, Peking University, Beijing 100871, China
Received 2024 December 31; revised 2025 March 10; accepted 2025 March 24; published 2025 May 9

Abstract

Recent JWST observations have revealed that dwarf galaxies start to cease star formation at redshifts $z > 1$, yet the quenching process remains unclear. In this study, we selected a large sample of 3405 dwarf galaxies with stellar masses below $10^{9.5} M_{\odot}$ and redshifts ranging from 1.0 to 1.5 across all five CANDELS fields. By utilizing multi-wavelength imaging data from both JWST and HST, we examined the growth patterns and modes of star formation quenching in dwarf galaxies during the cosmic noon era. Based on their specific star formation rates (sSFR), we categorized the sample into three subgroups: star-forming dwarf galaxies below and above the star formation main sequence (SFMS), and quiescent dwarf galaxies. To analyze the *UVJ* color profiles of these three subgroups of dwarf galaxies, we applied the image stacking technique. This method improves the signal-to-noise ratio and extends the color profiles to the outer regions of the galaxies. Our results show that these galaxies generally exhibit nearly flat stacked color profiles, suggesting that, on average, their growth and star formation quenching patterns are self-similar, differing from those previously observed in dwarf galaxies at lower redshifts. We further discuss the potential roles of internal and external physical processes in the star formation quenching of dwarf galaxies during the cosmic noon period.

Key words: galaxies: high-redshift – galaxies: dwarf – galaxies: star formation

1. Introduction

Over the past decade, the evolutionary path of massive galaxies, which dominate the stellar content of the universe, has been well understood through the observation of high-redshift progenitors of local massive galaxies (Pérez-González et al. 2008; Faisst 2015; Jing et al. 2021). However, for dwarf galaxies, which constitute the largest population of galaxies, comprehensive studies are limited to those at low redshifts (Cano-Díaz et al. 2022; Pharo et al. 2022). Beyond redshift $z \sim 1$, due to observational constraints, studies of dwarf galaxies have been restricted to case studies and small samples with specific characteristics, which limits a comprehensive understanding of the evolutionary paths of dwarf galaxies (van der Wel et al. 2011; Alavi et al. 2021; Gelli et al. 2021; Carniani et al. 2024). At intermediate to high redshifts, for massive galaxies, their spatially resolved properties can be accurately determined based on HST multi-band high-resolution imaging or spectroscopic observations, which aids in understanding how massive galaxies are built up and shut down (Liu et al. 2016, 2017; Nelson et al. 2016b, 2016a, 2021; Wang et al. 2017; Liu et al. 2018). However, for high-redshift dwarf galaxies, due to their small size and faint luminosity, there are few reliable spatially resolved statistical results.

Color gradients reflect the stellar population (age, specific star formation rate (sSFR), metallicity, etc.) and dust attenuation gradients within a galaxy (Gonzalez-Perez et al. 2011; Guo et al. 2011). The stellar population gradients can provide essential clues to understand how galaxies are built up and shut down (Lian et al. 2017). Several studies based on color gradients indicate that the growth and quenching modes of galaxies depend on stellar mass. On average, for massive galaxies, an inside-out growth and quenching mode is suggested (Liu et al. 2016; Wang et al. 2017; Abdurro'uf & Akiyama 2018; Liang & Li 2018; Tacchella et al. 2018; Jafariyazani et al. 2019); in contrast, for low-mass galaxies, a self-similar growth mode and an outside-in quenching mode are implied (Pan et al. 2015; Liang & Li 2018; Liu et al. 2018). The growth mode of galaxies reflects processes such as gas accretion from the cosmic web, cooling, and structural formation, thereby offering clues about the assembly history of galaxies. The quenching mode, on the other hand, reveals the dominant quenching mechanisms at play within galaxies. Generally, quenching mechanisms can be categorized into two types: internal and external. Internal quenching processes, including active galactic nucleus (AGN) feedback (Fabian 2012), supernova feedback (Geach et al. 2014), halo quenching (Birnboim & Dekel 2003; Dekel & Birnboim 2006; Gobat et al. 2015),

morphological quenching (Martig et al. 2009; Genzel et al. 2014; Zhang et al. 2019), central compaction (Fang et al. 2013; Lang et al. 2014; Tacchella et al. 2016; Barro et al. 2017; Faisst et al. 2017; Suess et al. 2020), and secular quenching processes, lead to an inside-out quenching pattern. External processes, such as ram pressure stripping caused by environmental effects (Abadi et al. 1999; Roediger & Hensler 2005; Boselli et al. 2022; Samuel & Pardasani 2023) and gas strangulation (Peng et al. 2015), strip gas starting from the outer regions, resulting in an outside-in quenching pattern. Overall, studying the color gradients in star-forming, quenching, and quenched galaxies can provide insights into the growth and quenching mechanisms driving these galaxies.

According to the downsizing scenario, dwarf galaxies evolve more slowly due to their shallower gravitational potential well (Cowie et al. 1996). Thus, on average, dwarf galaxies quench later than their more massive counterparts (Bell et al. 2004; Thomas et al. 2005; Faber et al. 2007; Walters et al. 2022). Determining when dwarf galaxies begin to quench is crucial for providing a comprehensive understanding of the evolution of the mass assembly history of galaxies and the corresponding dark matter halos. Based on the recent JWST PRIMER and UNCOVER surveys, Cutler et al. (2024) found that quiescent dwarf galaxies do indeed appear at cosmic noon. These galaxies exhibit a flatter mass-size relationship compared to their more massive counterparts, suggesting different formation pathways. Spatially resolved information, such as color gradients, is essential for further investigating the formation mechanisms of quenched dwarfs at high redshifts.

At low redshifts (e.g., $z < 1$), spatially resolved studies and environmental studies have led to the proposition of environmental quenching theories for dwarf galaxies (Peng et al. 2010; Geha et al. 2012; Chamba et al. 2024; Zheng et al. 2024). However, prior to the launch of the JWST, knowledge about the quenching mode of higher-redshift dwarf galaxies was very limited. Very recently, based on measurements of the sizes of quenched dwarf galaxies during cosmic noon, Cutler et al. (2024) proposed that stellar feedback and environmental effects might be key drivers of quenching in dwarf galaxies. These mechanisms are expected to play different roles. Due to the increase in star formation rates, it is anticipated that stellar and supernova feedback will be more significant at high redshifts (Tassis et al. 2003; Mashchenko et al. 2008; Clavijo-Bohórquez et al. 2024). Meanwhile, the clustering effect is likely to be relatively weaker at high redshifts. To gain a deeper understanding of the evolution of dwarf galaxies, spatially resolved studies of distant dwarf galaxies are essential, but such research remains very rare to date.

With the successful completion of the extragalactic deep field surveys by the JWST, we have been able to leverage its near-infrared camera NIRCAM to achieve a significant leap over the HST in terms of spatial resolution, observational depth, and wavelength coverage (Rieke et al. 2023; Rigby et al. 2023). These technological advancements have not only opened the door to in-depth exploration of the statistical properties of large samples of high-redshift dwarf galaxies but also allowed us to observe these distant faint galaxies with greater detail. In addition, stacking technology, as a powerful analytical tool, can extract the average signal of specific types of sources from noise, and this technique has been successfully applied to optical, infrared, and radio imaging data (Zibetti et al. 2004; Zheng et al. 2006; van der Wel et al. 2008; van Dokkum et al. 2010; Hancock et al. 2011; Tal & van Dokkum 2011; Guo et al. 2013; Wilson et al. 2017). By performing stacking analysis on the deep images captured by the JWST, we can determine the color gradients of distant dwarf galaxies out to large radius, which is of great significance for studying the growth and quenching modes of dwarf galaxies at high redshifts.

To investigate the growth and quenching modes of dwarf galaxies during cosmic noon, we have selected a sample of 3405 dwarf galaxies with stellar masses in the range $10^{8.0}M_{\odot} \leqslant M_{\star} \leqslant 10^{9.5}M_{\odot}$ between redshifts 1.0 and 1.5 from all five CANDELS fields (COSMOS, EGS, GOODSN, GOODSS, UDS). This mass range ensures completeness within our sample. At these redshifts, the angular diameter distance remains nearly constant, as shown in Figure 1, allowing us to disregard image and PSF resampling effects. We classify the sample into three categories based on their sSFR relative to the star formation main sequence (SFMS) and perform stacking analysis separately for each subgroup. For each stacked population, we derive *UVI* color profiles to infer the growth and quenching modes of dwarf galaxies.

This paper is structured as follows: Section 2.2 details the selection and classification of our galaxy sample. Section 2.3 outlines the methodology used in our stacking analysis. The results of this analysis are presented in Section 3. In Section 4, we compare our results with other studies and discuss potential biases in our work. Finally, we summarize our conclusions in Section 5. Throughout the paper, we adopt a cosmology with $\Omega_{\rm M} = 0.3$, $\Omega_{\Lambda} = 0.7$ and $H_0 = 70\,{\rm km\,s^{-1}\,Mpc^{-1}}$. All magnitudes are in the AB system.

2. Data and Method

2.1. The JWST Imaging Data

The JWST NIRCam imaging data from the CANDELS fields, sourced from the program of the Spatially Pixel-level Resolved Investigations into Nascent Galaxies with the James Webb Space Telescope (JWST-SPRING),[6] are utilized in this study. This program aims to provide the astronomical community with extensive, homogeneous, and deep imaging data from JWST's NIRCam and MIRI, as well as spectroscopic

[6] http://groups.bao.ac.cn/jwst_spring/

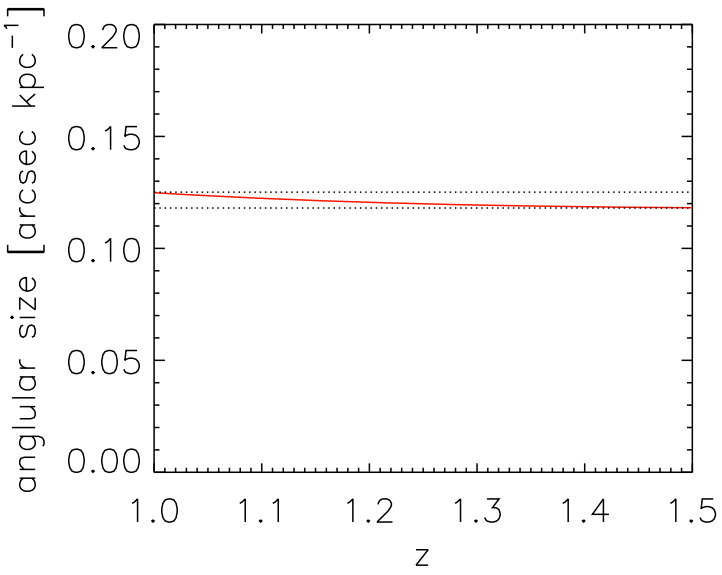

Figure 1. The relationship between redshift and angular size per kiloparsec. The bottom dashed line shows the angular size per kiloparsec at $z = 1.5$, and the top dashed line shows the 6% division from that at $z = 1.5$. It can be seen that the variance of the angular size per kiloparsec does not exceed 6% at the redshift range $1 < z < 1.5$.

data from NIRSpec and NIRCam/WFSS, all precisely matched with observations from the HST. The NIRCam data processing procedure is briefly summarized as follows:

We initiated our data reduction by processing the uncalibrated raw images from individual exposures using the Stage 1 pipeline, Detector1Pipeline, with its default configuration. This stage performs essential detector-level corrections, including a series of initial adjustments such as group scale correction, data quality initialization, superbias subtraction, reference pixel correction, linearity correction, persistence correction, dark current subtraction, jump detection, and gain scale correction. In particular, we have adopted an improved method similar for identifying "snowballs"—unusual cosmic ray events—and expanding their footprints. We then re-run the ramp-fitting step to generate count-rate maps that exclude the regions labeled as snowballs.

We proceeded to the Stage 2 pipeline, Image2Pipeline, on the count-rate images using default parameters. This critical stage encompasses WCS assignment, flat-fielding, and photometric calibration, resulting in fully calibrated individual exposures. Subsequently, we applied a series of bespoke corrections aimed at mitigating specific features. These corrections address scattered-light effects, such as wisps and claws, manage 1/f noise, and implement additional masking to enhance data quality. We have implemented masks to address various features that imprint on the mosaics, including persistence effects, dragon breath, ginkgo leaf patterns, uncorrected wisp features, and other artifacts. To ensure comprehensive coverage, we conducted a visual examination of all Stage 2 images to identify any residual artifacts. Additionally, we identified certain moving targets within the images and applied masking accordingly.

We then executed the Stage 3 pipeline, Image3Pipeline, to generate a unified mosaic for each filter of every observation. This process integrated all calibrated images from various dither positions and detectors. During this stage, we performed astrometric alignment to ensure precise spatial correspondence, background matching for visual consistency, outlier detection to maintain data integrity, and resampling of images onto a unified output grid for seamless integration. Finally, a customized background subtraction routine was reapplied to the individual mosaics before the co-added mosaics were created.

It is noted that our JWST scientific data have undergone pixel-level homogenization with HST observational images, and they exhibit greater precision in the correction of various instrumental effects than the scientific data released by other JWST teams. Specifically, to avoid over-subtraction of the background, we have implemented a meticulous sky background estimation and subtraction process. These data offer unique advantages for the study of the faint outskirts of massive galaxies and the low-mass dwarf galaxies. A detailed overview of the JWST-SPRING program will be provided in F. S. Liu et al. (2025, in preparation). The scientific imaging data in all five CANDELS fields and the homogeneous processing will be presented in Q. F. Cui et al. (2025, in preparation). More information about the JWST-SPRING imaging data can be found on the website.[7]

[7] https://sail-c.github.io/jwst-spring/

Table 1
Sample Selection Criteria and Sample Sizes

Criterion	COSMOS	EGS	GOODSN	GOODSS	UDS	TOTAL
$1.0 \leqslant z \leqslant 1.5$						
PhotFlag $= 0$	1395	2198	2307	2295	2133	10328
GALFIT Flag(H) $= 0$						
CLASS_STAR < 0.9						
$10^{8.0}M_{\odot} \leqslant M_{*} \leqslant 10^{9.5}M_{\odot}$	1078	1590	1607	1658	1486	7419
Good multi-band data and regular morphology	680	518	504	600	1103	3405

2.2. Catalogs and Sample Selection

Our sample is based on the CANDELS survey (Grogin et al. 2011; Koekemoer et al. 2011). Multi-band photometry catalogs were compiled by Nayyeri et al. (2017), Stefanon et al. (2017), Barro et al. (2019), Guo et al. (2013), and Galametz et al. (2013). The redshifts used are the best available, prioritized in the following order: secure spectroscopic redshifts, good grism redshifts, and photometric redshifts. Photometric redshifts are estimated by using a hierarchical Bayesian method to combine the results from 11 different codes based on the multi-wavelength photometry catalogs (Dahlen et al. 2013). Grism redshifts are from the 3D-HST survey (Morris et al. 2015; Momcheva et al. 2016). Spectroscopic redshifts were collected by N. Hathi (2025, private communication). Rest-frame magnitudes were estimated from the best redshift and multi-wavelength photometry catalogs by utilizing the EAZY (Brammer et al. 2008) software. Stellar masses were computed as the median values from 10 different teams, based on the best redshifts and the multi-wavelength catalog (Santini et al. 2015). Star formation rates (SFRs) were calculated based on dust-corrected rest-frame UV luminosities at 2800 Å (Kennicutt & Evans 2012). The dust correction was applied using the Calzetti et al. (2000) attenuation law and a foreground dust screen assumption. SFRs derived from dust-corrected UV luminosities are consistent with those derived from UV+IR luminosities across a broad mass range, except for very massive galaxies (Fang et al. 2018), which are not included in our sample. The attenuation A_V is the median value of the results of stellar population synthesis four methods (see labeled $2a\tau$,$12a$,$13a\tau$,$14a$ in Santini et al. 2015). These methods are based on the same assumptions of stellar population models (Bruzual & Charlot 2003), Chabrier (2003) IMF, and Calzetti et al. (2000) attenuation law, but differ in the code, star formation history, and metallicity assumptions. Morphological parameters, including the Sérsic index, effective radius, axis ratio, and position angle, were obtained from the catalog built by van der Wel et al. (2012), based on measurements of HST/F160W images using GALFIT (Peng et al. 2002).

In order to maximize the sample size and obtain high signal-to-noise ratio (SNR) stacked images, we select dwarf galaxies from all five CANDELS fields. The selection criteria are as follows:

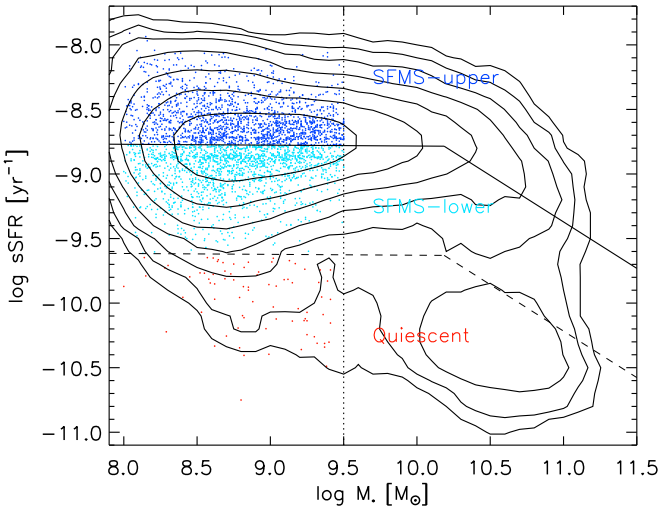

Figure 2. The relationship between sSFR and stellar mass for our sample galaxies. The SFMS is fitted using a broken power-law based on the entire sample. The contour illustrates the number density of galaxies on the M_{*}–sSFR plane. Our sample of dwarf galaxies is categorized into three subgroups based on their relative positions with respect to the SFMS, each color-coded accordingly. The blue points represent the dwarf galaxies above the SFMS, the cyan points represent the dwarf galaxies below the SFMS, and the red points represent the quiescent dwarf galaxies.

1. Photflag $= 0$ to ensure that the photometry is reliable and spurious sources are removed.
2. CLASS_STAR $\leqslant 0.9$ to reduce contamination by point sources.
3. GALFIT $f_{\rm H} = 0$ to select galaxies with relatively regular morphology.
4. Redshift between 1.0 and 1.5 to control the variation in angular diameter distance, thereby allowing us to omit the resampling of images and PSF.
5. Stellar mass in the range of $8.0 \leqslant \log(M_{\star}/M_{\odot}) \leqslant 9.5$ to obtain a complete sample of dwarf galaxies. Mass completeness is ensured for stellar masses above $10^{8.0}M_{\odot}$, and galaxies with stellar masses below $10^{9.5}M_{\odot}$ can be defined as dwarf galaxies (Reines 2022).
6. Multi-band images in HST/ACS (F606W, F814W) and JWST/NIRCam (F115W, F150W, F200W, F277W,

Table 2
Sample Sizes of the Subgroups Used for Stacking

Classification	COSMOS	EGS	GOODSN	GOODSS	UDS	TOTAL
mr SFMS-upper	454	314	223	175	542	1708
SFMS-lower	214	180	267	412	545	1618
Quiescent	12	24	14	13	16	79

F356W, F444W) are available and not contaminated by the borders of the mosaic, bad pixels, asterisms, or bright sources.

7. Sources with irregular surface brightness profiles indicative of mergers are excluded. We visually inspect the multi-band images and exclude those sources with irregular structure(merger-like, double-core, multi-core, etc.).

Table 1 lists our selection criteria and the resulting sample sizes after each selection step for each field. We obtain 3405 dwarf galaxies from all five CANDELS fields before classification.

Figure 2 illustrates the relationship between sSFR and stellar mass for our sample of galaxies. Consistent with previous research findings, the SFMS is better constrained by a broken power-law rather than a single power-law (Whitaker et al. 2014; Tomczak et al. 2016). At the higher mass end, the slope becomes shallower. This broken power-law is defined by five parameters: the slope and zero-point at both the low-mass and high-mass ends, and the critical mass at which the slope changes. We employ a 3σ clipping method to fit the best SFMS relationship for *UVJ*-selected star-forming galaxies from the entire sample. The best-fit broken power-law is displayed in Figure 2 and is described by the following equations: $\log \mathrm{sSFR}/\mathrm{yr}^{-1} = -0.01 \pm 0.01[\log(M_*/M_\odot)] - 8.72 \pm 0.17$ for $\log(M_*/M_\odot) \leqslant 10.19$ and $\log \mathrm{sSFR}/\mathrm{yr}^{-1} = -0.72 \pm 0.16[\log(M_*/M_\odot)] - 1.45 \pm 0.10$ for $\log(M_*/M_\odot) > 10.19$.

As shown in Figure 2, on the number density contour plot of sSFR versus stellar mass, we observe that at the low-mass end, the distribution of sSFR does not exhibit the bimodality seen at the high-mass end. Instead, the distribution shows a single peak along the SFMS and extends outwards to a skewed tail toward the quiescent population. Based on the relative values of sSFR to the SFMS, we categorize the dwarf galaxy samples into three subgroups: dwarf galaxies above the SFMS, dwarf galaxies below the SFMS, and the quiescent population. The specific definitions of these three subgroups are as follows:

1. The SFMS-upper group consists of dwarfs that lie above the SFMS but within the 3σ upper limit of the SFMS.
2. The SFMS-lower group includes dwarfs that are below the SFMS but still above the 3σ lower limit of the SFMS.
3. The quiescent population comprises dwarfs with sSFRs below the 3σ lower limit of the SFMS.

Table 3
SExtractor Parameters for Masking Companion Sources

Parameter	Value
DETECT_MINAREA	25
DETECT_THRESHOLD	0.75
ANALYSIS_THRESHOLD	3.0
DEBLEND_NTHRESH	64
DEBLEND_MINCONT	0.001

The sample sizes for these subgroups are detailed in Table 2. Specifically, our final sample for stacking analysis includes 1708 galaxies in the SFMS-upper group, 1618 in the SFMS-lower group, and 79 in the quiescent group.

2.3. Stacking Analysis

To investigate the average surface brightness profiles and color gradients of the three subgroups of dwarf galaxies, we perform a stacking analysis on multi-band images for each subgroup separately. The detailed procedure for this analysis is outlined below.

2.3.1. Image Cut-out Extraction

Given the celestial coordinates of our galaxy sample and the astrometric information of the images, we extract image cut-outs by centering all galaxies within the cut-out images. This ensures that the centers of all galaxies are aligned, enabling a pixel-by-pixel stacking procedure. The cut-out images have a width of 301 pixels, corresponding to a physical diameter of approximately $\sim$75 kpc. This size is large enough to accommodate subsequent processing steps, including image rotation and background subtraction for dwarf galaxies.

2.3.2. Source Masking

To eliminate contamination from sources unrelated to the target galaxies, it is necessary to mask companion sources. To create deep and reliable masks applicable to all bands, we co-add images across all eight bands. We then run SExtractor (Bertin & Arnouts 1996) on these co-added images to generate a segmentation map, using the parameters listed in Table 3. In the segmentation map, pixels that do not correspond to the background (value 0) or the target galaxy (value at the center)

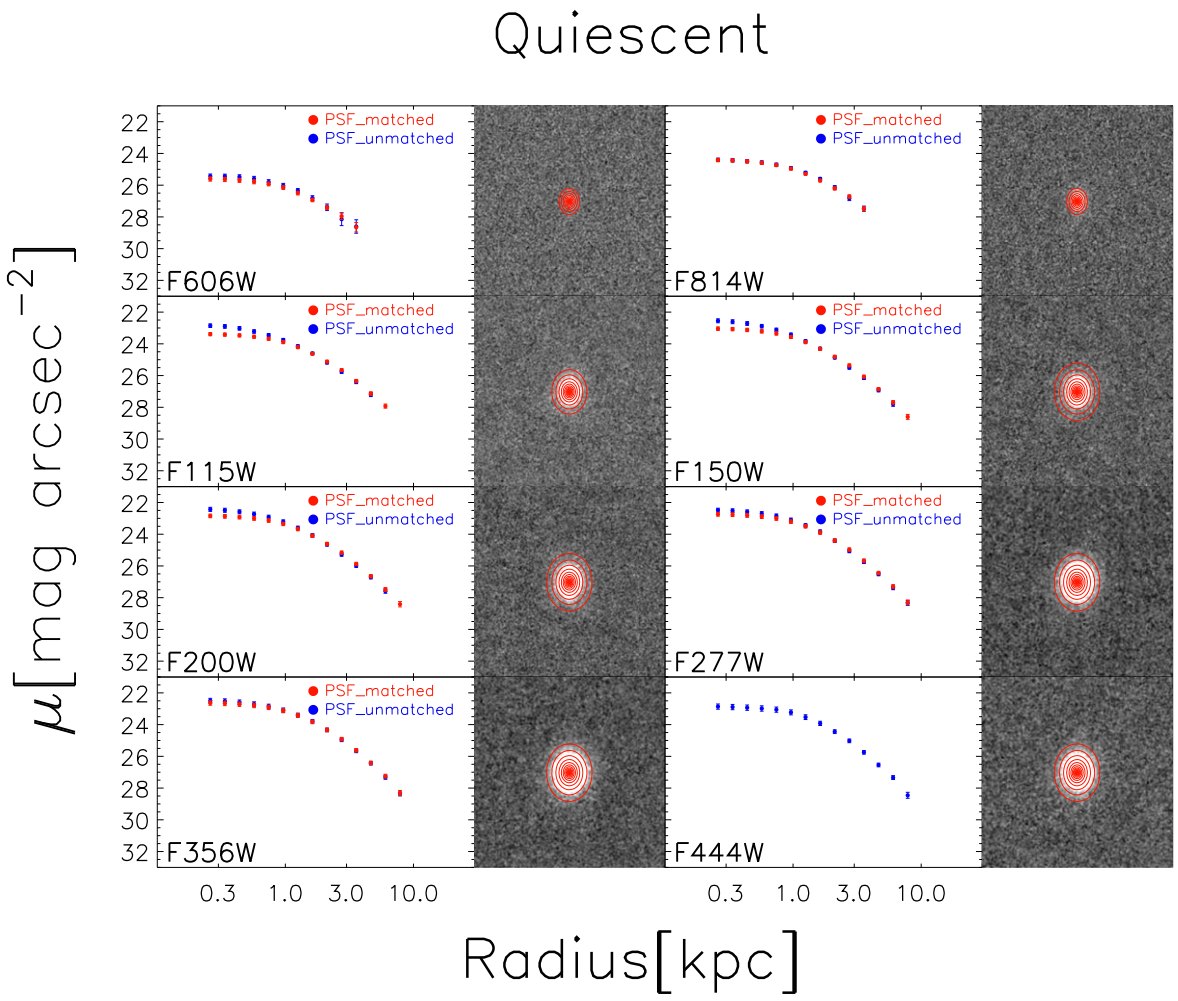

Figure 3. The stacked surface brightness profiles for the quiescent dwarf galaxies across various bands. The blue points correspond to the original surface brightness profiles, whereas the red points indicate the profiles after PSF matching to the F444W filter.

are masked. These masked pixels are excluded from contributing to the final stacked image.

2.3.3. Background Subtraction

Accurate background subtraction is critical to obtain reliable signals, particularly at the outskirts of galaxies. We employ a median filtering window with a width of 71 pixels to construct background images from unmasked background pixels. The filter size, approximately 17 kpc, is about 10 times the typical effective radius of dwarf galaxies, making it suitable for cleanly removing the background. A detailed evaluation of the background subtraction process is provided in Appendix A.

2.3.4. Image Rotation

To minimize anisotropy in different directions, we rotate the galaxy images such that their major axes are aligned. This is achieved using the IDL program `hrot.pro` in the IDL Astronomy User's Library.[8] The algorithm is analogous to the rotation algorithm implemented in the IRAF task GEOTRAN, which has been demonstrated to be effective in stacking procedures (D'Souza et al. 2014).

2.3.5. Cosmic Dimming Correction

To render the surface brightness profiles of galaxies at different redshifts comparable, it is necessary to correct for cosmic dimming effects. Following the method of Wang et al. (2019), we multiply each processed image by $(1 + z)^4/(1 + 1.25)^4$ to adjust the cosmic dimming effect to a common redshift of $z = 1.25$, which corresponds to the median value of the redshift range under investigation.

[8] https://asd.gsfc.nasa.gov/archive/idlastro/

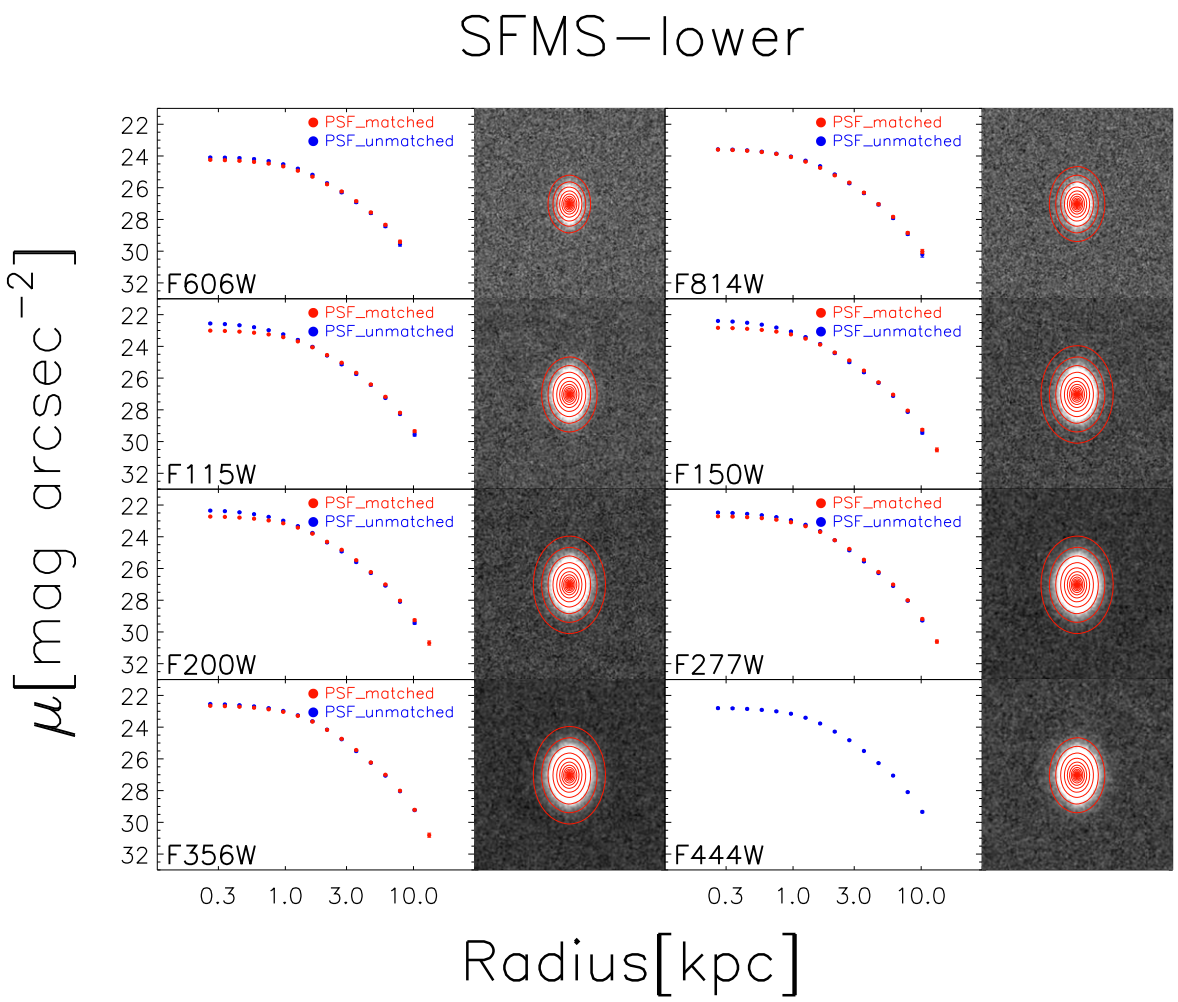

Figure 4. Same as Figure 3 but for the dwarf galaxies below the SFMS.

2.3.6. Image Stacking

We stack the images at each band for each subgroup separately. For each pixel, the final value is computed as the 3σ-clipped averaged value of all input images at the corresponding location without mask. The clipping procedure removes outliers and smooths the stacked images. As suggested by Wang et al. (2019), varying the discarding fraction between 1% and 10% does not bias the stacking results. Given that the angular diameter distance remains nearly constant across the redshift range, we do not resample the images to a common grid of pixels with the same physical scale.

2.3.7. PSF Matching

To avoid false color gradients arising from variations in the point-spread function (PSF) between different bands, we PSF-match the stacked images to the F444W image, the PSF of which has the largest full width at half maximum (FWHM).

2.3.8. Surface Brightness Profile Measurement

We measure the surface brightness profiles of the multi-band stacked images using elliptical apertures with the IRAF task `ellipse`. The apertures share the same center, position angle, and ellipticity, with radii increasing in logarithmic steps. The ellipticity of the stacked images is derived from the parameters determined by SExtractor (Bertin & Arnouts 1996) on the F444W stacked image, and the position angles are aligned as described in Section 2.3.4.

2.3.9. Error Estimation

We employ the bootstrapping method to estimate the statistical errors. This statistical error is based on 50 bootstrap samples, each generated by randomly selecting galaxies with a sample size identical to the original sample. The standard deviation of these 50 bootstrap samples serves as an estimate of the statistical error.

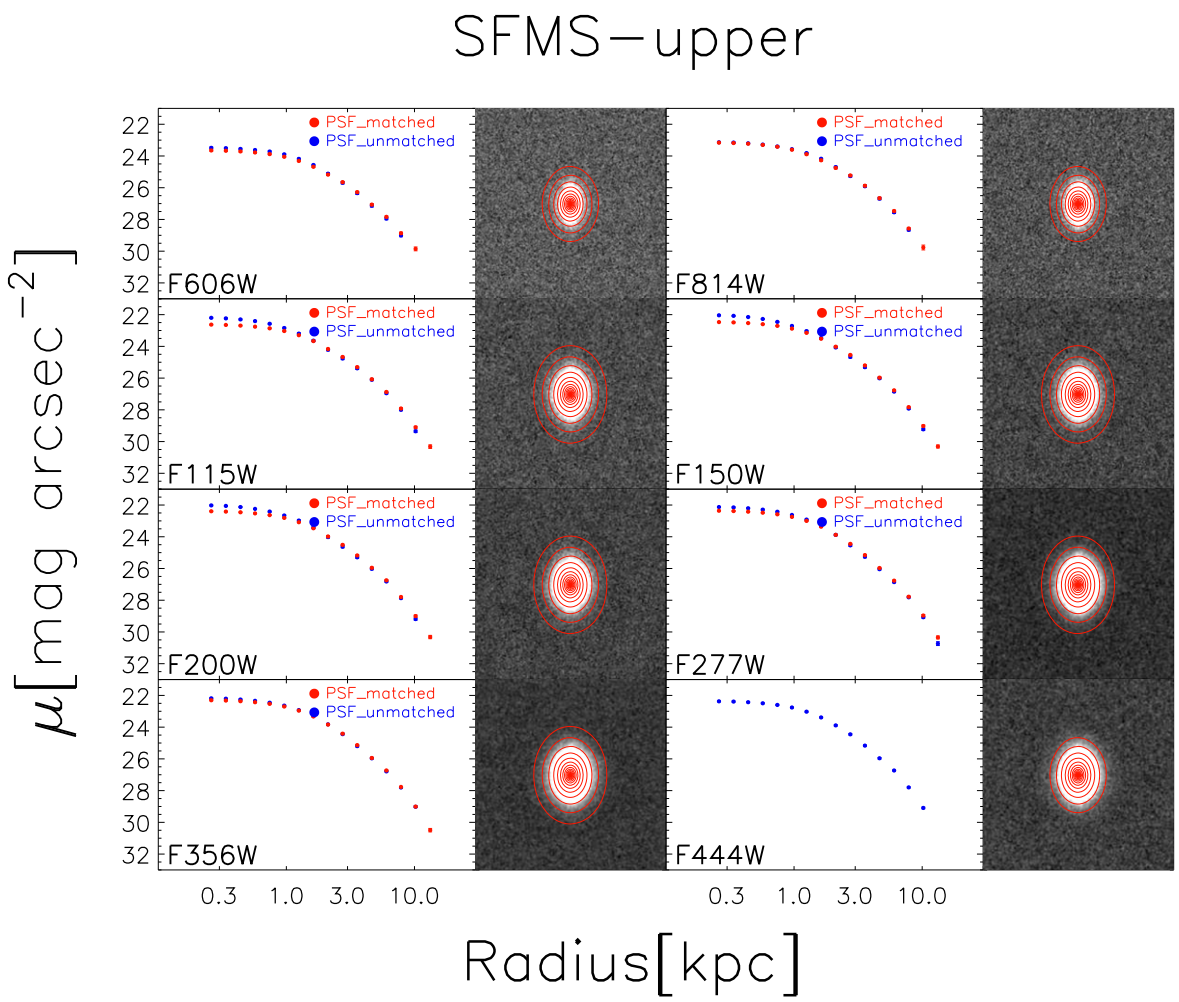

Figure 5. Same as Figure 3 but for the dwarf galaxies above the SFMS.

2.3.10. Rest-frame Color Gradients

To derive the rest-frame color gradients, which reflect the gradients of star formation activity, we utilize EAZY (Brammer et al. 2008) to interpolate the observed-frame surface brightness profiles to the rest-frame. The redshift is fixed at $z = 1.25$, which is the median value of the redshift range in our study.

3. Results and Analysis

3.1. The Surface Brightness Profiles

Figures 3, 4, and 5 display the stacked surface brightness profiles for each subgroup across eight bands. The average surface brightness profiles that we determined for dwarf galaxies are smooth and extend to about 10 kpc, several times the typical effective radius of dwarf galaxies. Furthermore, by comparing surface brightness profiles between different bands, it is evident that the profiles based on JWST images are about 1 mag deeper than those based on HST images, highlighting the immense potential of using JWST images and image stacking techniques to study the faint structures of galaxies. We also observe that the stacked surface brightness profiles of star-forming galaxies above and below the SFMS can extend to larger radii than those of quiescent dwarfs. This phenomenon can be partly attributed to sample size. Since the SNR is proportional to the square root of the sample size, the depth of the stacked images increases with a larger sample size. On the other hand, actively star-forming dwarf galaxies may possess larger radii, and their sizes shrink once star formation ceases, a characteristic similar to the quenching process in massive galaxies (Fang et al. 2018). Overall, the greater extent of the surface brightness profiles demonstrates the power of deep JWST image stacking. Detailed comparisons and discussions of the stacking effects can be found in Appendix A.

In Figure 6, we compare the stacked surface brightness profile of the three subgroups at each band. The differences in the surface brightness profile become smaller as the wavelength

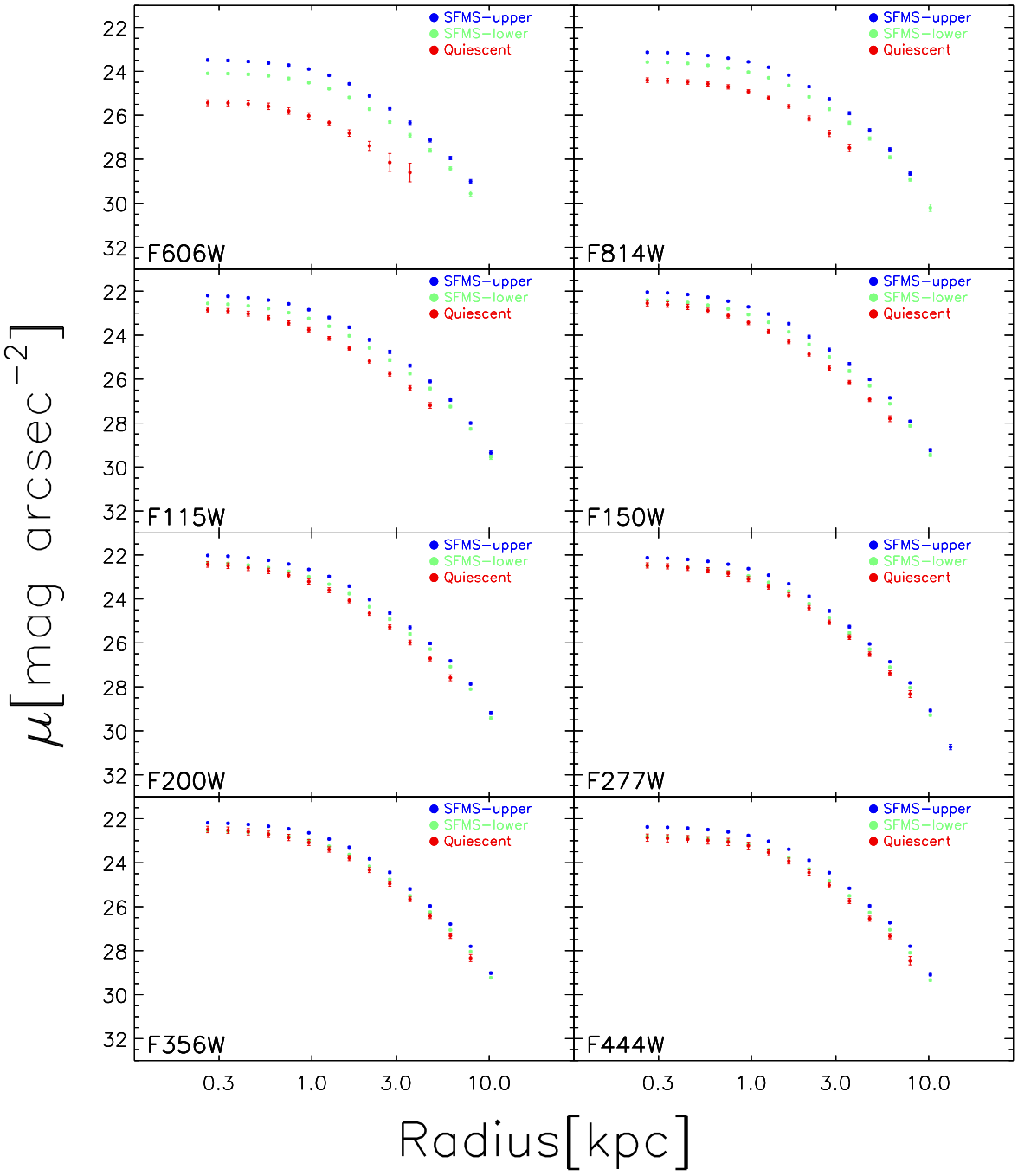

Figure 6. The comparison of the stacked surface brightness profile of the quiescent, SFMS-lower, and SFMS-upper at each band. As the wavelength becomes longer, the discrepancy of the surface brightness profile becomes smaller.

increases, suggesting that the mass-to-light variation at different bands dominates the discrepancy of the surface brightness profile. At F200W, F277W, F356W, F444W bands, corresponding to the rest-frame near-infrared wavelength, which can trace the stellar mass profile, the surface brightness profile is similar. It is suggested that the galaxies do not experience violent structure transformation during the growth and quenching process.

3.2. *The* U − V *Color Profiles*

The color index $U - V$ is an effective indicator for tracing the age of stellar populations and dust content in galaxies. Given that

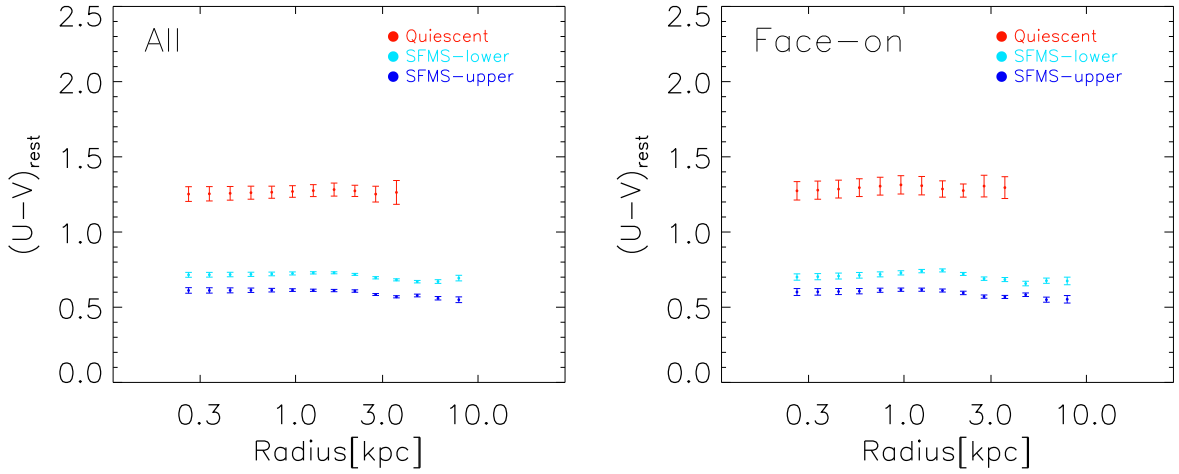

Figure 7. The stacked $U-V$ color profiles of quiescent dwarf galaxies, as well as those below and above the SFMS, are presented separately. Notably, all subgroups exhibit a flat color profile, which suggests a self-similar, gradual quenching process. The left panel shows the stacked results without any restriction of the inclination angle, and the right panel shows the stacked results when only face-on subsamples are included.

dwarf galaxies contain minimal dust, we use uncorrected rest-frame $U-V$ color gradients directly to infer the gradients of stellar populations. As shown in the left panel of Figure 7, the $U-V$ color profiles for these three subgroups are flat. The flat $U-V$ color gradients suggest that dwarf galaxies between redshifts 1.0 and 1.5 grow and quench in a self-similar manner. This finding implies that the internal structure of these dwarf galaxies does not significantly change with radius, indicating consistent evolutionary processes across different regions within the galaxies during the quenching process.

To assess the extent to which dust attenuation and projection effects might influence our results, we also selected face-on dwarf galaxies with an axis ratio of 0.5 or greater and stacked them separately into the SFMS-upper, SFMS-lower, and quiescent populations. As shown in the right panel of Figure 7, the results remain largely unchanged. This consistency demonstrates that the observed flat color gradients accurately reflect the intrinsic stellar population gradients, free from significant impacts of dust attenuation and projection effects.

3.3. *The* UVJ *Color Trajectories*

The UVJ color–color diagram has proven to be an effective tool for disentangling the effects of dust attenuation from those of sSFR degeneracies (Williams et al. 2009; Whitaker et al. 2011; Fang et al. 2018). In this section, we further explore how dwarf galaxies are represented on the *UVJ* diagram, reinforcing our understanding of the role that dust extinction plays in these systems. Figure 8 displays the *UVJ* color gradients of star-forming galaxies above and below the SFMS and the quiescent population. Our observations reveal that for quiescent dwarf galaxies, there is no significant change in $U-V$ and $V-J$ colors from the center to the outskirts up to 3 kpc. For star-forming galaxies on either side of the SFMS, $U-V$ colors fluctuate within the error range, and $V-J$ colors change only about 0.15 to 0.2 mag from the center to approximately 7 kpc, indicating that the $V-J$ color gradient ($d(V-J)/d\log(r)$) in star-forming dwarf galaxies remains fairly shallow, not exceeding 0.35. These findings suggest that the influence of dust extinction gradients does not significantly affect our primary conclusions regarding the properties of these galaxies. Additionally, studies have shown that at higher redshifts, dwarf galaxies tend to exhibit elongated morphologies rather than being dominated by disk structures (van der Wel et al. 2014). Consequently, the ellipticity of these galaxies may not fully represent their optical depth, which in turn further explains the observed color uniformity.

4. Discussion

How, when, and why dwarf galaxies quench is a critical question for understanding the evolutionary history of this most populous group of galaxies. At low redshifts, studies based on color gradients have revealed that the quenching of dwarf galaxies follows an outside-in pattern associated with environmental effects (Pan et al. 2015; Liang & Li 2018; Liu et al. 2018). Studies based on environmental parameters show that in the low-redshift universe, quenched dwarf galaxies predominantly exist in dense environments, supporting the idea that environmental effects are primarily responsible for quenching in this context (Peng et al. 2010; Geha et al. 2012; Guo et al. 2017; Kawinwanichakij et al. 2017). We also note that for low-redshift dwarf galaxies, AGN activity and surface density Σ_1 are related to the quenching process, indicating that internal processes cannot be ignored in the quenching of dwarf galaxies (Cai et al. 2020, 2021; Guo et al. 2021; Arjona-Gálvez et al. 2024).

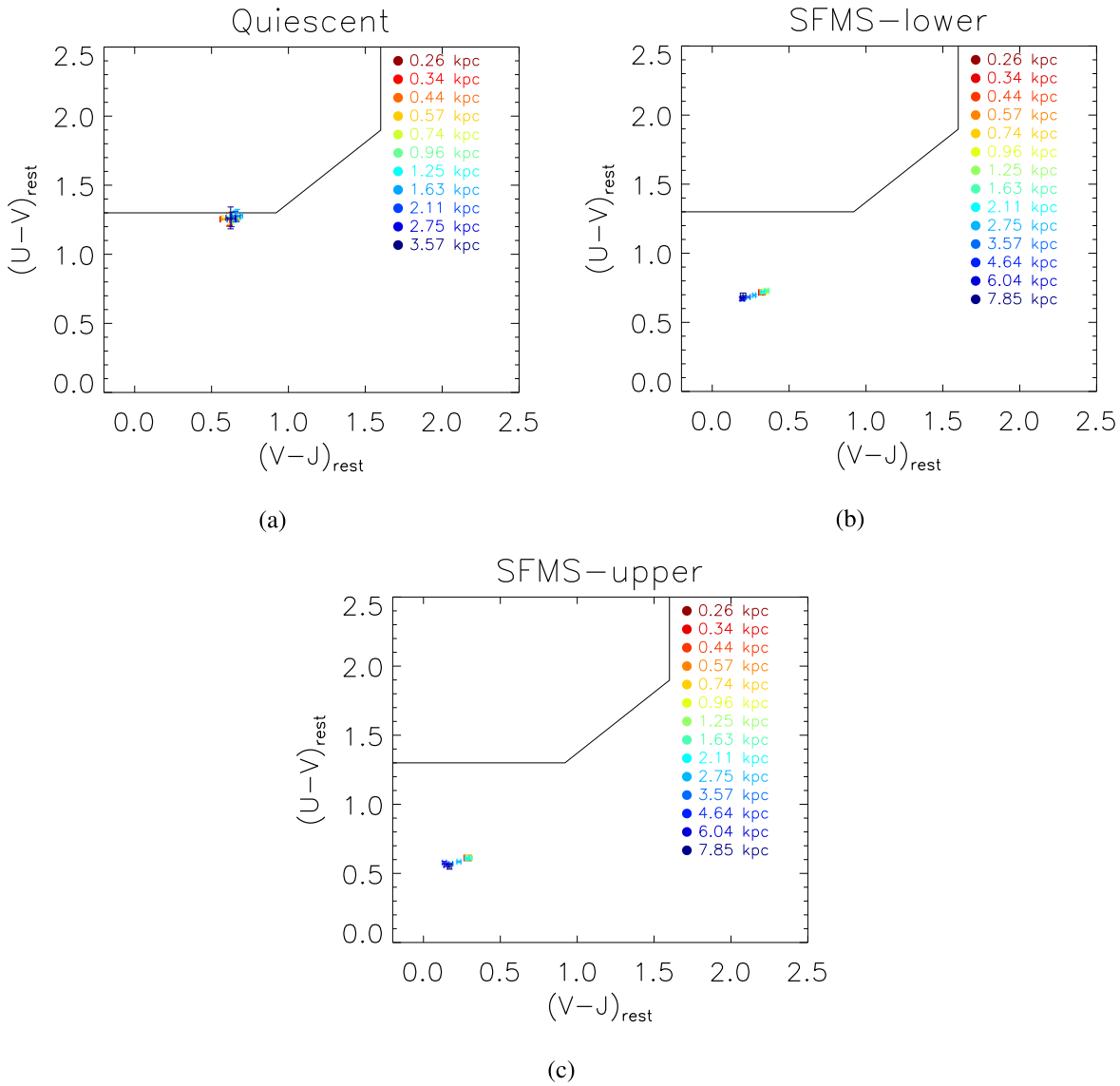

Figure 8. The stacked *UVJ* color trajectories of dwarf galaxies on the *UVJ* plane. Panel (a) shows the UVJ color trajectories for quiescent dwarf galaxies, panel (b) shows that for the dwarf galaxies below the SFMS, and panel (c) shows that for the dwarf galaxies above the SFMS. The line represents the separation between the quiescent galaxies and star-forming galaxies at $1 < z < 1.5$ following (Williams et al. 2009). For quiescent dwarf galaxies, the positions on the UVJ diagram remain largely consistent from the central regions to the outskirts, indicating minimal variation in the color trajectories across the galaxy on average. For the dwarf galaxies lying above and below the SFMS, the overall color gradient is relatively small, indicating only a slight variation in *UVJ* colors across the galaxy.

At high redshifts, the lack of a complete large sample with spectroscopic redshift observations limits the study of the environments of dwarf galaxies. Based on a sample of 12 post-starburst dwarf galaxies with redshifts between 3 and 6, Alberts et al. (2024) found that these galaxies reside in overdense regions, suggesting that environmental effects still play a role for dwarf galaxies at higher redshifts. By leveraging the advantages of deep JWST image stacking, our study reveals that at $z > 1$, the quenching mode of dwarf galaxies differs significantly from that at lower redshifts. They exhibit self-similar quenching patterns rather than the outside-in mode observed in local dwarf galaxies. The results indicate that as redshift increases, the influence of the environment on the quenching of dwarf galaxies decreases and is no longer the dominant quenching mechanism beyond redshift 1. This scenario is related to the evolution of clustering effects.

Additionally, McGee et al. (2014) proposed a quenching model called "overconsumption," wherein galaxies cease star formation due to outflows driven by star formation or AGN

feedback, which rapidly deplete the remaining gas reservoirs when the gas supply is interrupted. Our results support the overconsumption model over the ram pressure stripping model because star formation-driven outflows naturally produce flat sSFR gradients during quenching (El-Badry et al. 2016; Belfiore et al. 2018), whereas ram pressure stripping would lead to an outside-in quenching pattern (Lin et al. 2019). Therefore, the overconsumption model seems to reasonably explain the formation mechanisms of quenched dwarf galaxies at redshifts $z > 1$. However, it should be noted that we cannot rule out the possibility that multiple quenching mechanisms may act simultaneously. At high redshifts, external environmental impacts weaken compared to those at lower redshifts, but they may play a comparable role to internal quenching mechanisms, leading to self-similar quenching patterns. Further research is needed to clarify this issue.

Given that at the low-mass end, the distribution of sSFR does not exhibit the clear bimodality seen in more massive galaxies, there is an ongoing debate about whether these "quenched dwarfs" are truly "fully quenched" or only "partially quenched," that is, whether they might return to a state of star formation (Strait et al. 2023; Dome et al. 2024; Looser et al. 2024). The skewed distribution of sSFR provides evidence that "fully quenched" dwarf galaxies dominate our sample; however, to definitively prove this point, a larger statistical sample is needed to examine the evolutionary pattern of the number density of quenched dwarf galaxies (Lundgren et al. 2014; Martis et al. 2016; Weaver et al. 2023), which is beyond the scope of this work.

Furthermore, major mergers represent an important quenching mechanism linked to environmental effects (Feldmann et al. 2010; Gabor et al. 2010; Kado-Fong et al. 2024). In this study, we have excluded potential mergers and disturbed galaxies from our analysis, which means we are unable to evaluate the role of major mergers in the quenching process of dwarf galaxies. Future investigations into the merger rates of dwarf galaxies could offer valuable insights into this issue. Moreover, major mergers frequently occur in dense regions, therefore, our sample may have some potential bias against dense regions, where environmental effects could play a more significant role. Regardless, our observational findings demonstrate that in relatively sparse regions, dwarf galaxies generally quench in a self-similar manner.

5. Summary

In this work, we have carefully selected a large sample of dwarf galaxies within the redshift range of 1–1.5 and measured their average surface brightness profiles and color profiles using image stacking techniques to investigate their growth and quenching modes. In this redshift range, the mass completeness of dwarf galaxies can be assured, and the physical scale for a specific pixel remains nearly constant. This latter characteristic simplifies the normalization process as it allows us to neglect the resampling of images and PSFs. Our study reveals that, on average, dwarf galaxies at the cosmic noon exhibit flat color profiles regardless of whether they reside on the SFMS or have been quenched. This implies that during this epoch, dwarf galaxies grow and quench in a self-similar mode, which differs from the self-similar growth and outside-in quenching patterns observed in dwarf galaxies at lower redshifts. Moreover, our results suggest that environmental effects and internal processes may play common roles in the quenching of dwarf galaxies beyond redshift $z = 1$, implying a combined influence rather than dominance by a single process during this epoch. This phenomenon is associated with the evolution of the environment and internal feedback processes linked to star formation activity.

Our research demonstrates the powerful capability of stacking JWST images to study the average spatially resolved properties of small and faint sources. The stacking method employed in this paper provides an efficient approach for investigating objects with insufficient SNR. By utilizing the stacking technique on JWST images, galaxy studies can be extended to higher redshifts and lower masses, thereby constructing a more comprehensive picture of galaxy evolution.

Acknowledgments

This work is supported by the National Natural Science Foundation of China (NSFC, grant Nos. 12273052, 11733006, 12090040, 12090041 and 12073051), and the science research grants from the China Manned Space Project (No. CMS-CSST-2021-A04). N.L. acknowledges the support from the Ministry of Science and Technology of China (No. 2020SKA0110100), the science research grants from the China Manned Space Project (No. CMS-CSST-2021-A01), and the CAS Project for Young Scientists in Basic Research (No. YSBR-062). This work is supported by the National Key R&D Program (2023YFE0101200), the China Manned Space Project (No. CMS-CSST-2025-A07), the NSFC (grant No. 12393813), and the Yunnan Revitalization Talent Support Program (YunLing Scholar Project).

Appendix A
The Effect of Background Subtraction and the Enhancement of Signal-to-Noise Ratio by Stacking

Background estimation and subtraction are crucial yet challenging for studying the color gradients of galaxies, especially at the outskirts of faint sources. Over-subtraction can lead to the loss of signal associated with the outer regions of the source, while under-subtraction may result in background contamination of the signal. Given the size of dwarf galaxies, we employed a median filter with a window size of

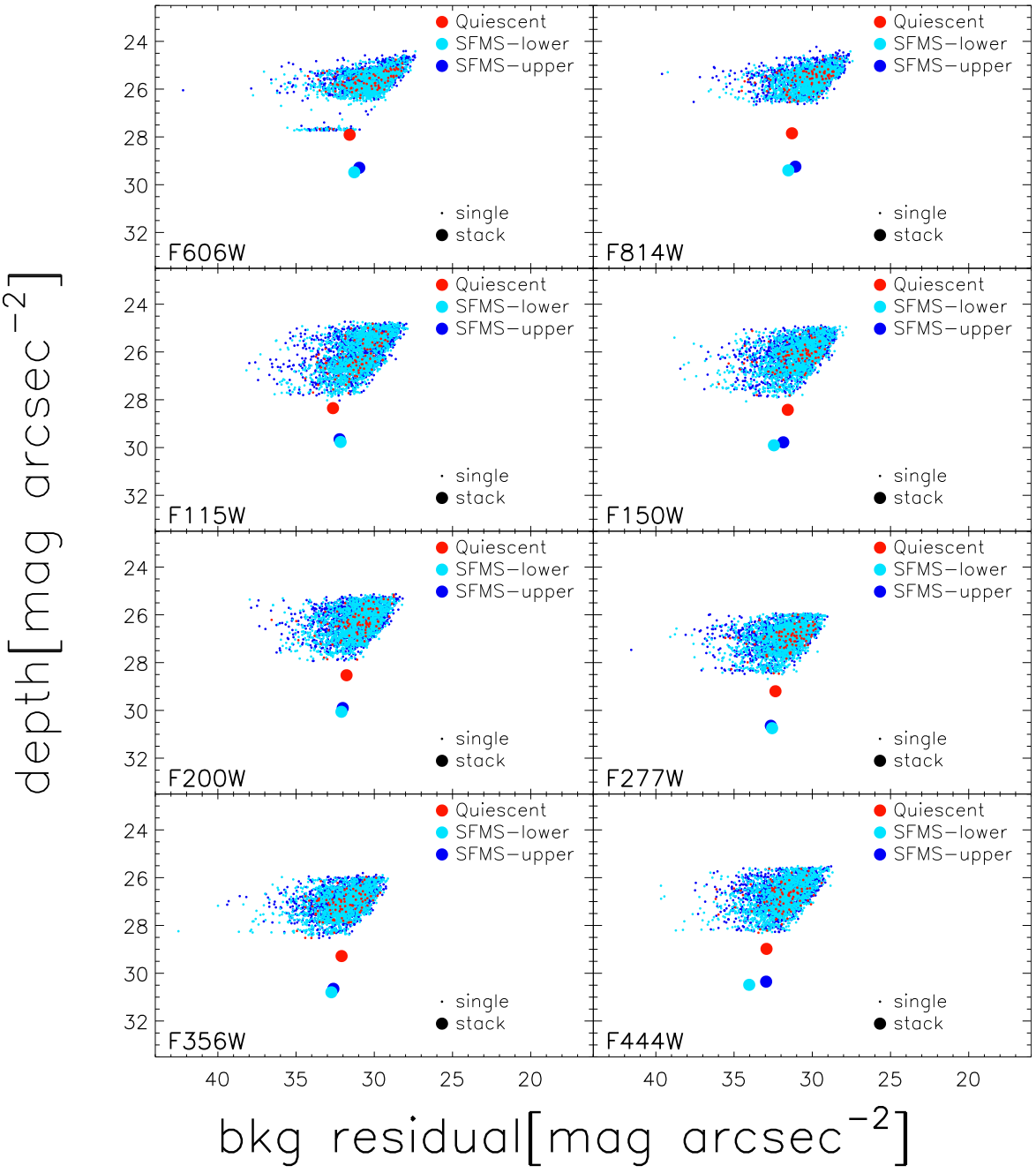

Figure A1. Comparison of background residuals and fluctuations in single images vs. stacked images. After our background subtraction, the residual background level can reach approximately 33 mag arcsec^{-2} . After stacking procedure, the depth of the images increases by 2∼4 mag, which is consistent with theoretical predictions.

71 pixels to construct a background map, which was subsequently subtracted from the images. To assess the effectiveness of our background estimation and subtraction, we performed statistical analyses on the background-subtracted images. Our findings indicate that after background subtraction, the residual background level remains below 28 mag arcsec^{-2}. On average, this residual is 5 mag dimmer than the background fluctuations, demonstrating a clean and effective background subtraction process.

Fundamentally, the enhancement of the SNR is proportional to the square root of the sample size. Given that we adjust the images to account for the cosmic dimming effect, making surface brightnesses comparable, rather than using inverse variance weighting, the resulting SNR is slightly less than what

would be ideal. To assess the improvement in SNR achieved through stacking, we compare the background statistics of single images with those of the stacked images. Figure A1 illustrates that the stacked image achieves a depth 2 mag greater for quiescent galaxies and 4 mag greater for star-forming galaxies. This outcome is consistent with theoretical predictions, validating the efficacy of our stacking procedure.

Appendix B
The Robustness of the Stacking Procedure

To test the robustness of the stacking procedure, we compare the stacked average surface brightness profile with the surface brightness profiles of individual sources. Figures B1, B2, and B3 illustrate the results. We observe that the surface brightness profile derived from the stacked image aligns well with the median surface brightness profile of individual sources up to the radius where more than 90% of single sources can be measured. This consistency demonstrates that the stacking procedure does not introduce any additional systematic bias in determining the surface brightness profile.

At the outskirts of galaxies, only the surface brightness profiles of brighter sources can typically be measured for individual targets. The stacking process mitigates this bias toward bright sources by including targets with low surface brightness at the outskirts as well. Consequently, the stacking method provides a more comprehensive and accurate representation of surface brightness profiles, especially for fainter regions.

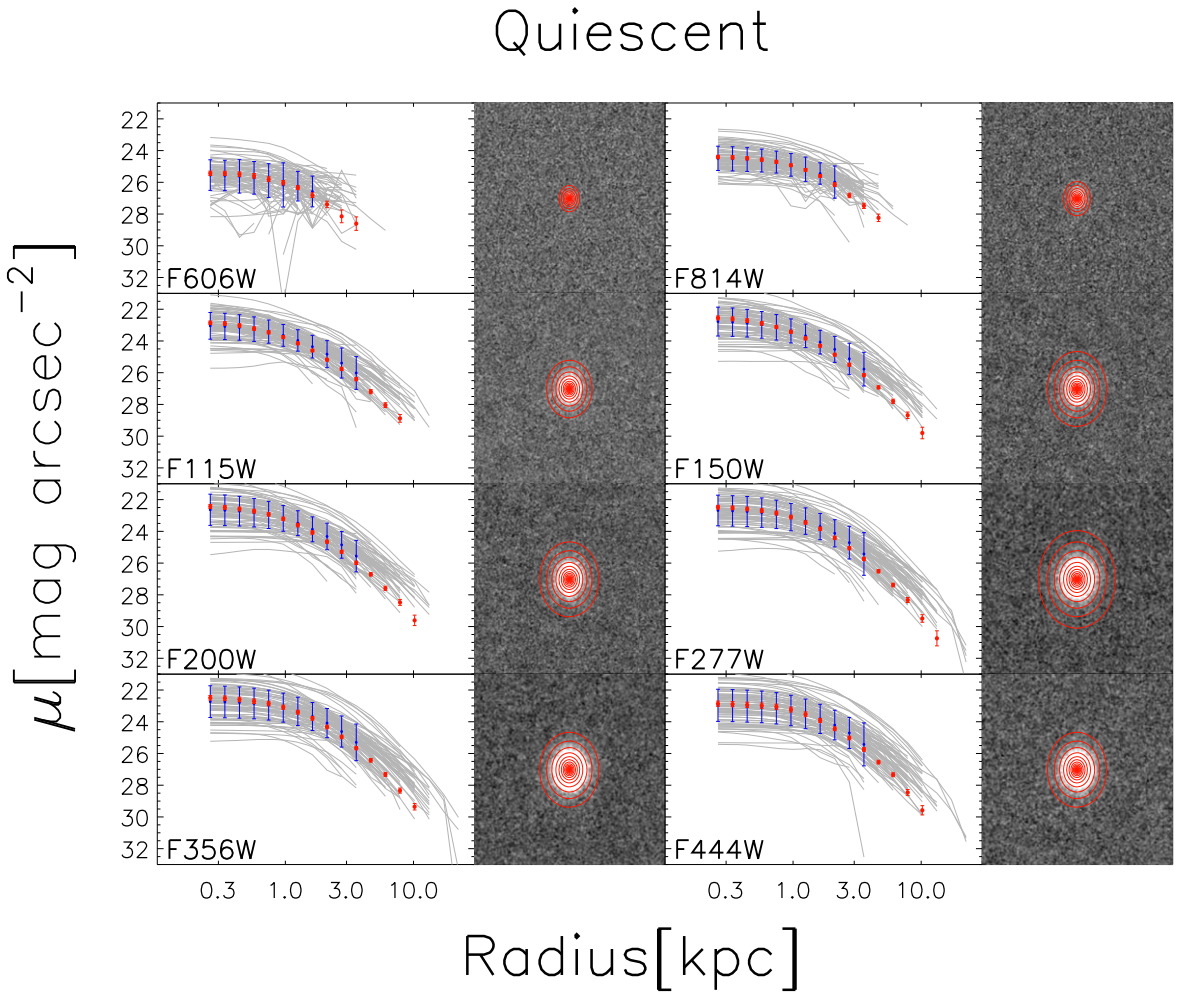

Figure B1. Comparison of surface brightness profiles for single targets and stacked images in each band for quiescent dwarf galaxies. The gray lines depict the surface brightness profiles of individual targets. The blue points represent the median surface brightness profile of single targets where 90% completeness is ensured, while the red points illustrate the surface brightness profile of the stacked images. It is evident that in the inner regions, the stacked surface brightness profile aligns well with the median surface brightness profile of individual objects. At the outskirts, only the surface brightness profiles of brighter sources can typically be measured for single targets. However, the stacked surface brightness profile incorporates information from all sources, thereby avoiding any bias toward brighter targets. This approach ensures a more inclusive and accurate representation of the surface brightness at larger radii, highlighting the advantages of the stacking method in capturing detailed structural information of galaxies.

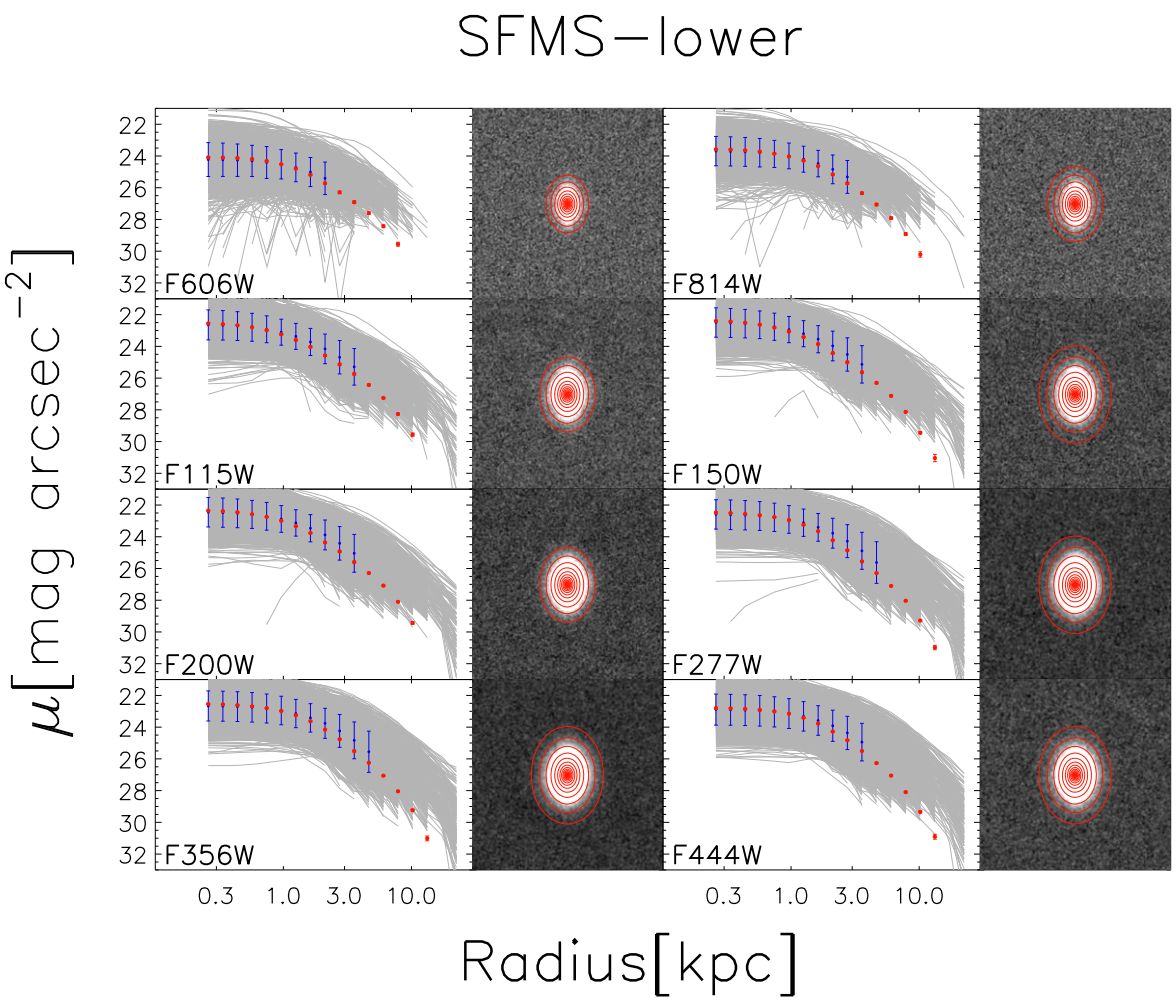

Figure B2. Same as Figure B1 but for the dwarf galaxies below the SFMS.

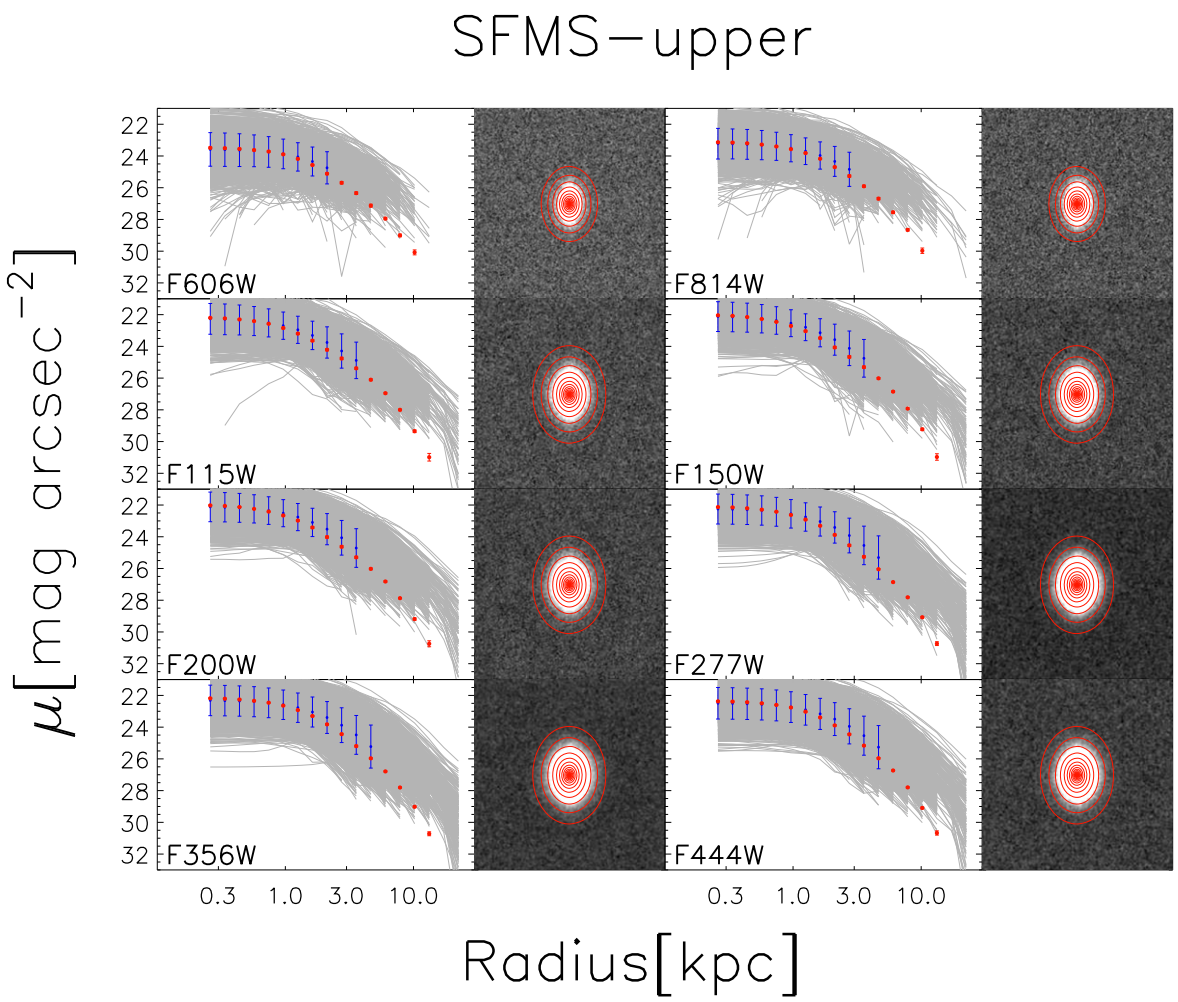

Figure B3. Same as Figure B1 but for the dwarf galaxies above the SFMS.

Appendix C
The Dependence of Color Profile on Stellar Mass and Redshift

In our study, to increase the SNR, we do not split the sample into several redshift and stellar mass bins to make the sample size as large as possible. But the color gradients are dependent on stellar mass and redshift (Liu et al. 2016, 2017; Wang et al. 2017; Liu et al. 2018). Considering that our sample spreads over a large stellar mass and redshift range, we further check whether the flat color profiles are caused by the smoothing effect of the evolution of color gradients and the dependence of color gradients on stellar mass. We split the sample into two stellar mass and two redshift bins and stack them separately. Sample sizes of each stellar mass and redshift bin are listed in Table C1 for each subgroup. The results are shown in Figure C1. We can see that, even after the splitting, the color profile remains flat, indicating that the flat stacked color profile is not caused by the variations of the color profiles for individual galaxies over a large stellar mass and redshift bin. We note that, for quiescent galaxies, since the sample size is small, after dividing the quiescent galaxies by stellar mass and redshift, the SNR is not enough to resolve the intrinsic profile. The color profile of the stacked image can be measured only out to 1 kpc, which is similar to the FWHM of the PSF at the F444W band.

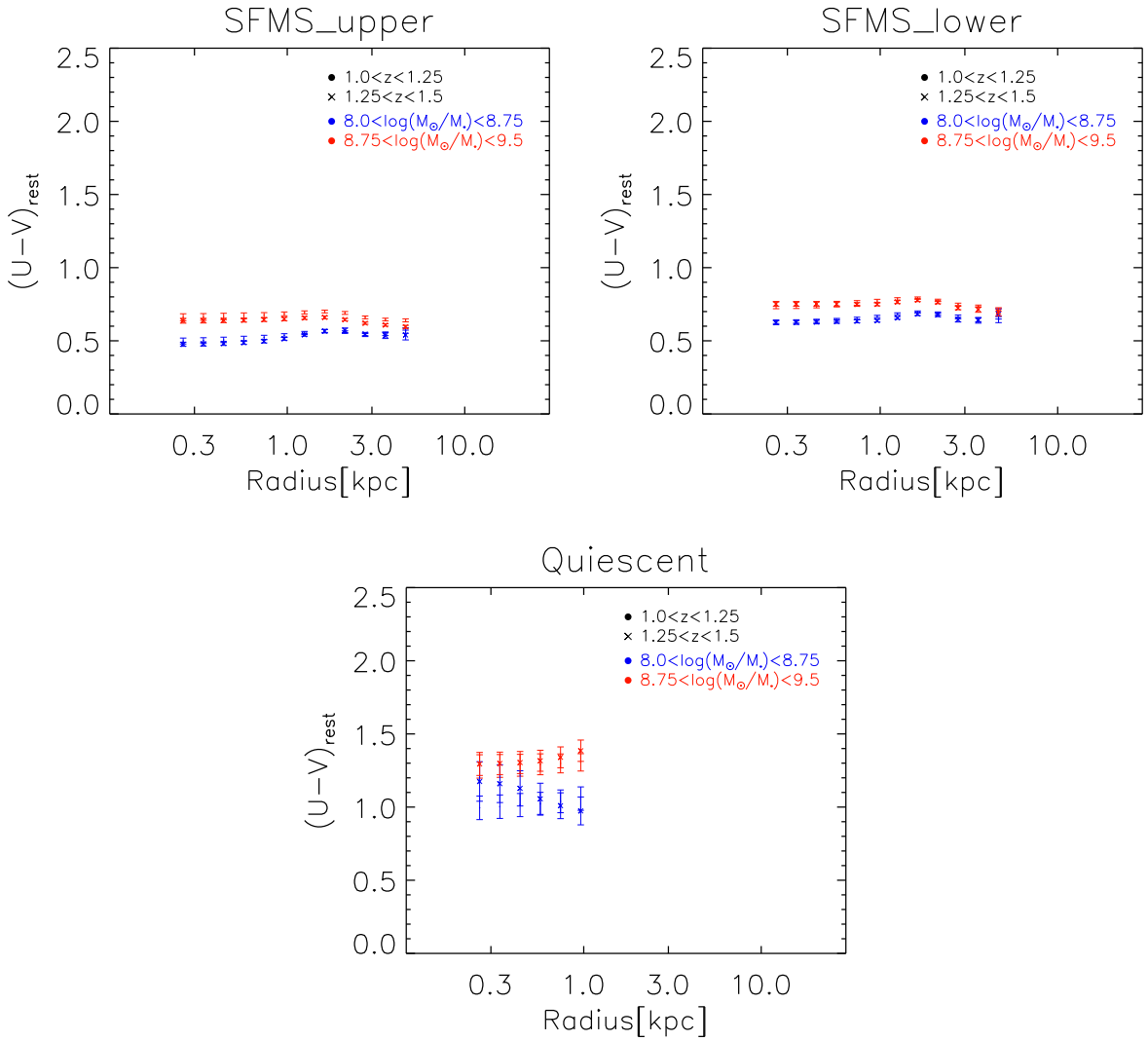

Figure C1. The stacked rest-frame $U - V$ color profile of the dwarf galaxies for each stellar mass and redshift bin. For the dwarf galaxies above and below the SFMS, it can be seen that the stacked color profile remains flat after splitting into smaller stellar mass and redshift bins. For the quiescent dwarf galaxies, due to the limitation of the sample size, the color profile can be only measured out to 1 kpc, which is similar to the FWHM of the PSF at the F444W band.

Table C1
Sample Sizes of Each Stellar Mass and Redshift Bin for Each Subgroup

	$1.0 \leqslant z \leqslant 1.25$			$1.25 \leqslant z \leqslant 1.5$		
	SFMS_upper	SFMS_lower	Quiescent	SFMS_upper	SFMS_lower	Quiescent
$10^{8.0}M_{\odot} \leqslant M_{*} \leqslant 10^{8.75}M_{\odot}$	384	459	21	407	338	5
$10^{8.75}M_{\odot} \leqslant M_{*} \leqslant 10^{9.5}M_{\odot}$	360	439	37	557	382	16

ORCID iDs

Yubin Li https://orcid.org/0000-0002-4882-1057
Qi Song https://orcid.org/0009-0007-5833-3210

References

Abadi, M. G., Moore, B., & Bower, R. G. 1999, MNRAS, 308, 947
Abdurro'uf, & Akiyama, M. 2018, MNRAS, 479, 5083
Alavi, A., Colbert, J., Teplitz, H., et al. 2020, ApJ, 904, 59
Alberts, S., Williams, C. C., Helton, J. M., et al. 2024, ApJ, 975, 85
Arjona-Gálvez, E., Di Cintio, A., & Grand, R. J. J. 2024, A&A, 690, A286
Barro, G., Faber, S. M., Koo, D. C., et al. 2017, ApJ, 840, 47
Barro, G., Pérez-González, P. G., Cava, A., et al. 2019, ApJS, 243, 22
Belfiore, F., Maiolino, R., Bundy, K., et al. 2018, MNRAS, 477, 3014
Bell, E. F., Wolf, C., Meisenheimer, K., et al. 2004, ApJ, 608, 752
Bertin, E., & Arnouts, S. 1996, A&AS, 117, 393
Birnboim, Y., & Dekel, A. 2003, MNRAS, 345, 349
Boselli, A., Fossati, M., & Sun, M. 2022, A&ARv, 30, 3
Brammer, G. B., van Dokkum, P. G., & Coppi, P. 2008, ApJ, 686, 1503
Bruzual, G., & Charlot, S. 2003, MNRAS, 344, 1000
Cai, W., Zhao, Y., Zhang, H.-X., et al. 2020, ApJ, 903, 58
Cai, W., Zhao, Y.-H., & Bai, J.-M. 2021, RAA, 21, 204
Calzetti, D., Armus, L., Bohlin, R. C., et al. 2000, ApJ, 533, 682
Cano-Díaz, M., Hernández-Toledo, H. M., Rodríguez-Puebla, A., et al. 2022, AJ, 164, 127
Carniani, S., Venturi, G., Parlanti, E., et al. 2024, A&A, 685, A99
Chabrier, G. 2003, PASP, 115, 763
Chamba, N., Marcum, P. M., Saintonge, A., et al. 2024, ApJ, 974, 247
Clavijo-Bohórquez, W. E., de Gouveia Dal Pino, E. M., & Melioli, C. 2024, MNRAS, 535, 1696
Cowie, L. L., Songaila, A., Hu, E. M., et al. 1996, AJ, 112, 839
Cutler, S. E., Whitaker, K. E., Weaver, J. R., et al. 2024, ApJL, 967, L23
Dahlen, T., Mobasher, B., Faber, S. M., et al. 2013, ApJ, 775, 93
Dekel, A., & Birnboim, Y. 2006, MNRAS, 368, 2
Dome, T., Tacchella, S., Fialkov, A., et al. 2024, MNRAS, 527, 2139
D'Souza, R., Kauffman, G., Wang, J., et al. 2014, MNRAS, 443, 1433
El-Badry, K., Wetzel, A., Geha, M., et al. 2016, ApJ, 820, 131
Faber, S. M., Willmer, C. N. A., Wolf, C., et al. 2007, ApJ, 665, 265
Fabian, A. C. 2012, ARA&A, 50, 455
Faisst, A. L., Carollo, C. M., Capak, P. L., et al. 2017, ApJ, 839, 71
Faisst, A. L. 2015, The evolution of star-forming and quiescent massive galaxies through cosmic time, PhD thesis, ETH Zurich
Fang, J. J., Faber, S. M., Koo, D. C., et al. 2013, ApJ, 776, 63
Fang, J. J., Faber, S. M., Koo, D. C., et al. 2018, ApJ, 858, 100
Feldmann, R., Carollo, C. M., Mayer, L., et al. 2010, ApJ, 709, 218
Gabor, J. M., Davé, R., Finlator, K., et al. 2010, MNRAS, 407, 749
Galametz, A., Grazian, A., Fontana, A., et al. 2013, ApJS, 206, 10
Geach, J. E., Hickox, R. C., Diamond-Stanic, A. M., et al. 2014, Natur, 516, 68
Geha, M., Blanton, M. R., Yan, R., et al. 2012, ApJ, 757, 85
Gelli, V., Salvadori, S., Ferrara, A., et al. 2021, ApJL, 913, L25
Genzel, R., Förster Schreiber, N. M., Lang, P., et al. 2014, ApJ, 785, 75
Gobat, R., Daddi, E., Bethermin, M., et al. 2015, IAUGA, 29, 2254506
Gonzalez-Perez, V., Castander, F. J., & Kauffmann, G. 2011, MNRAS, 411, 1151
Grogin, N. A., Kocevski, D. D., Faber, S. M., et al. 2011, ApJS, 197, 35
Guo, K., Zheng, X. Z., & Fu, H. 2013, ApJ, 778, 23
Guo, Y., Bell, E. F., Lu, Y., et al. 2017, ApJL, 841, L22
Guo, Y., Carleton, T., Bell, E. F., et al. 2021, ApJ, 914, 7
Guo, Y., Ferguson, H. C., Giavalisco, M., et al. 2013, ApJS, 207, 24
Guo, Y., Giavalisco, M., Cassata, P., et al. 2011, ApJ, 735, 18
Hancock, P. J., Gaensler, B. M., & Murphy, T. 2011, ApJL, 735, L35
Jafariyazani, M., Mobasher, B., Hemmati, S., et al. 2019, ApJ, 887, 204
Jing, Y.-J., Rong, Y., Wang, J., et al. 2021, RAA, 21, 218
Kado-Fong, E., Robinson, A., Nyland, K., et al. 2024, ApJ, 963, 37
Kawinwanichakij, L., Papovich, C., Quadri, R. F., et al. 2017, ApJ, 847, 134
Kennicutt, R. C., & Evans, N. J. 2012, ARA&A, 50, 531
Koekemoer, A. M., Faber, S. M., Ferguson, H. C., et al. 2011, ApJS, 197, 36
Lang, P., Wuyts, S., Somerville, R. S., et al. 2014, ApJ, 788, 11
Lian, J., Yan, R., Blanton, M., et al. 2017, MNRAS, 472, 4679
Liang, Z.-X., & Li, C. 2018, RAA, 18, 143
Lin, L., Hsieh, B.-C., Pan, H.-A., et al. 2019, ApJ, 872, 50
Liu, F. S., Jiang, D., Faber, S. M., et al. 2017, ApJL, 844, L2
Liu, F. S., Jiang, D., Guo, Y., et al. 2016, ApJL, 822, L25
Liu, F. S., Jia, M., Yesuf, H. M., et al. 2018, ApJ, 860, 60
Looser, T. J., D'Eugenio, F., Maiolino, R., et al. 2024, Natur, 629, 53
Lundgren, B. F., van Dokkum, P., Franx, M., et al. 2014, ApJ, 780, 34
Martig, M., Bournaud, F., Teyssier, R., et al. 2009, ApJ, 707, 250
Martis, N. S., Marchesini, D., Brammer, G. B., et al. 2016, ApJL, 827, L25
Mashchenko, S., Wadsley, J., & Couchman, H. M. P. 2008, Sci, 319, 174
McGee, S. L., Bower, R. G., & Balogh, M. L. 2014, MNRAS, 442, L105
Momcheva, I. G., Brammer, G. B., van Dokkum, P. G., et al. 2016, ApJS, 225, 27
Morris, A. M., Kocevski, D. D., Trump, J. R., et al. 2015, AJ, 149, 178
Nayyeri, H., Hemmati, S., Mobasher, B., et al. 2017, ApJS, 228, 7
Nelson, E. J., Tacchella, S., Diemer, B., et al. 2021, MNRAS, 508, 219
Nelson, E. J., van Dokkum, P. G., Förster Schreiber, N. M., et al. 2016a, ApJ, 828, 27
Nelson, E. J., van Dokkum, P. G., Momcheva, I. G., et al. 2016b, ApJL, 817, L9
Pan, Z., Li, J., Lin, W., et al. 2015, ApJL, 804, L42
Peng, C. Y., Ho, L. C., Impey, C. D., et al. 2002, AJ, 124, 266
Peng, Y., Maiolino, R., & Cochrane, R. 2015, Natur, 521, 192
Peng, Y.-j., Lilly, S. J., Kovač, K., et al. 2010, ApJ, 721, 193
Pharo, J., Guo, Y., Calvo, G. B., et al. 2022, ApJS, 261, 12
Pérez-González, P. G., Rieke, G. H., Villar, V., et al. 2008, ApJ, 675, 234
Reines, A. E. 2022, NatAs, 6, 26
Rieke, M. J., Kelly, D. M., Misselt, K., et al. 2023, PASP, 135, 028001
Rigby, J., Perrin, M., McElwain, M., et al. 2023, PASP, 135, 048001
Roediger, E., & Hensler, G. 2005, A&A, 433, 875
Samuel, J., & Pardasani, B. 2023, AAS, 241, 260.05
Santini, P., Ferguson, H. C., Fontana, A., et al. 2015, ApJ, 801, 97
Stefanon, M., Yan, H., Mobasher, B., et al. 2017, ApJS, 229, 32
Strait, V., Brammer, G., Muzzin, A., et al. 2023, ApJL, 949, L23
Suess, K. A., Kriek, M., Price, S. H., et al. 2020, ApJL, 899, L26
Tacchella, S., Carollo, C. M., Förster Schreiber, N. M., et al. 2018, ApJ, 859, 56
Tacchella, S., Dekel, A., Carollo, C. M., et al. 2016, MNRAS, 458, 242
Tal, T., & van Dokkum, P. G. 2011, ApJ, 731, 89
Tassis, K., Abel, T., Bryan, G. L., et al. 2003, ApJ, 587, 13
Thomas, D., Maraston, C., Bender, R., et al. 2005, ApJ, 621, 673
Tomczak, A. R., Quadri, R. F., Tran, K.-V. H., et al. 2016, ApJ, 817, 118
van der Wel, A., Bell, E. F., Häussler, B., et al. 2012, ApJS, 203, 24
van der Wel, A., Chang, Y.-Y., Bell, E. F., et al. 2014, ApJL, 792, L6
van der Wel, A., Holden, B. P., Zirm, A. W., et al. 2008, ApJ, 688, 48
van der Wel, A., Straughn, A. N., Rix, H.-W., et al. 2011, ApJ, 742, 111
van Dokkum, P. G., Whitaker, K. E., Brammer, G., et al. 2010, ApJ, 709, 1018
Walters, D., Woo, J., & Ellison, S. L. 2022, MNRAS, 511, 6126
Wang, W., Faber, S. M., Liu, F. S., et al. 2017, MNRAS, 469, 4063
Wang, W., Han, J., Sonnenfeld, A., et al. 2019, MNRAS, 487, 1580
Weaver, J. R., Davidzon, I., Toft, S., et al. 2023, A&A, 677, A184
Whitaker, K. E., Franx, M., Leja, J., et al. 2014, ApJ, 795, 104
Whitaker, K. E., Labbé, I., van Dokkum, P. G., et al. 2011, ApJ, 735, 86
Williams, R. J., Quadri, R. F., Franx, M., et al. 2009, ApJ, 691, 1879
Wilson, D., Cooray, A., Nayyeri, H., et al. 2017, ApJ, 848, 30
Zhang, C., Peng, Y., Ho, L. C., et al. 2019, ApJL, 884, L52
Zheng, X. Z., Bell, E. F., Rix, H.-W., et al. 2006, ApJ, 640, 784
Zheng, Y., Xu, K., Jing, Y. P., et al. 2024, ApJ, 969, 129
Zibetti, S., White, S. D. M., & Brinkmann, J. 2004, MNRAS, 347, 556